
Bridging Sequence and Graph Structure for Epigenetic Age Prediction

Yao Li

School of Computing and Information Systems
The University of Melbourne
yao.li5@student.unimelb.edu.au

Xikun Zhang*

School of Computing Technologies
RMIT University
xikun.zhang@rmit.edu.au

Xiaotao Shen

Lee Kong Chian School of Medicine
Nanyang Technological University Singapore
xiaotao.shen@ntu.edu.sg

Sonika Tyagi

School of Computing Technologies
RMIT University
sonika.tyagi@rmit.edu.au

Xin Zheng

School of Computing Technologies
RMIT University
xin.zheng2@rmit.edu.au

Jiaying Huang

Department of Data Science and Artificial Intelligence
Hong Kong Polytechnic University
jiaying.huang0508@outlook.com

Feng Xia

School of Computing Technologies
RMIT University
f.xia@ieee.org

Abstract

Epigenetic clocks based on DNA methylation have emerged as powerful tools for estimating biological age, with broad applications in aging research, age-related disease studies, and longevity science. Despite advances across machine learning approaches to epigenetic age prediction, spanning penalised linear regression, deep feedforward networks, residual architectures, and graph neural networks, no existing method jointly models co-methylation graph structure and site-specific DNA sequence context within a unified framework. We propose a unified sequence-graph integration framework for epigenetic age prediction that addresses this gap, integrating eight-dimensional DNA sequence statistical features through a lightweight gated modulation mechanism that adaptively scales each site’s methylation signal according to its sequence-determined biological relevance prior to graph convolution. Evaluated on 3,707 blood methylation samples against a comprehensive set of baselines, our method achieves a test MAE of 3.149 years, a 12.8% improvement over the strongest graph-based baseline. Biologically informed statistical features outperform CNN-based sequence encoding, demonstrating that handcrafted sequence features are more effective than end-to-end learned representations in this data regime. Post-hoc interpretability analysis identifies CpG density and local adenine frequency as features with age-dependent importance shifts, consistent with known mechanisms of age-related hypermethylation at CpG-dense promoter regions. Our code is at <https://github.com/yaoli2022/graphage-seq>.

*corresponding author

1 Introduction

Aging is one of the most significant biological processes impacting human health, yet its molecular mechanisms remain incompletely understood. DNA methylation, predominantly the addition of methyl groups to cytosines at cytosine-guanine dinucleotide (CpG) sites in mammals, is a major epigenetic mechanism through which cells regulate gene expression and maintain normal biological function [1]. By controlling which genes are transcriptionally active, methylation patterns underpin fundamental cellular processes including development, differentiation, and homeostasis. As individuals age, these patterns undergo systematic and reproducible changes, progressively disrupting the regulatory programmes that sustain cellular function and contributing to the emergence of age-related diseases such as neurodegeneration, cardiovascular disease, and cancer [2, 3, 4, 5]. The close coupling between methylation state and cellular functional status makes genome-wide methylation profiles a powerful molecular readout of biological age, and has motivated the development of epigenetic clocks as tools for precise biological age estimation, with broad applications in early disease diagnosis, therapeutic monitoring, and longevity research [6].

Existing epigenetic clocks fall into two broad categories based on how they represent CpG sites. The first treats CpG sites as independent features, spanning penalised linear regression on selected sites [2, 3] to deep learning architectures including feedforward networks and residual convolutional models that improve prediction accuracy by capturing non-linear methylation dynamics [7, 8]. Despite their improved accuracy, these methods discard the relational structure among CpG sites. The second category addresses this limitation by representing methylation data as a graph, where CpG sites are nodes and their relationships such as co-methylation, chromosomal proximity, and shared gene membership are edges, enabling graph neural networks to capture structural dependencies that flat feature vectors cannot [9, 10]. Despite this progress, no existing method jointly models co-methylation graph structure and site-specific DNA sequence context, leaving a fundamental gap that our work addresses.

Existing epigenetic clock models share two fundamental limitations that have not been addressed simultaneously. First, most methods treat CpG sites as independent features, discarding the rich relational structure among them. Co-methylation, the tendency of spatially proximate or functionally related CpG sites to exhibit correlated methylation states, encodes biologically significant information about chromatin organisation and transcriptional regulation that flat feature vectors cannot capture [11]. Second, no existing method incorporates the local DNA sequence context of each CpG site into its representation. The sequence environment surrounding a CpG site is a primary determinant of its methylation susceptibility: sequence-level properties such as GC content, CpG density, and local nucleotide composition govern DNA methyltransferase enzyme binding preferences [12, 13] and directly shape age-related methylation dynamics. These limitations are fundamentally coupled: without sequence context, the model cannot identify which relational structure is biologically meaningful, and without graph structure, sequence-informed signals cannot propagate across functionally related sites [14].

We assert that a principled solution requires a unified framework that jointly integrates co-methylation graph structure and site-specific DNA sequence context. Graph neural networks naturally capture relational structure by enabling each CpG site to aggregate information from its neighbours, while sequence features provide the site-specific biological context that determines each site’s regulatory significance. The key challenge lies in effectively integrating these two sources of information: methylation signals vary across individuals and drive supervised learning, whereas sequence features are site-specific biological priors that are invariant across individuals and cannot be optimised through standard supervision, requiring a dedicated mechanism to bridge this information.

This work proposes a unified sequence–graph integration framework for epigenetic age prediction. CpG sites are represented as nodes in a graph with edges encoding co-methylation relationships, chromosomal proximity, and shared gene membership. For each node, an eight-dimensional statistical feature vector encoding GC content, CpG density, and local nucleotide composition is integrated through a lightweight gated modulation mechanism that adaptively scales each site’s methylation signal according to its sequence-determined biological relevance before graph convolution. We further compare two sequence encoding strategies, demonstrating that biologically informed statistical features outperform CNN-based one-hot encoding in this data regime. Our main contributions are as follows:

- **Joint sequence and graph integration.** We propose the first unified framework that simultaneously models co-methylation graph structure and site-specific DNA sequence context for epigenetic age prediction, achieving a test MAE of 3.149 years and surpassing all evaluated baselines including classical epigenetic clocks, deep learning predictors, and graph-based methods.
- **Gated sequence modulation.** We introduce a lightweight gated mechanism that adaptively scales each site’s methylation signal according to its sequence-determined biological relevance, yielding an 18.1% MAE improvement over the sequence-agnostic baseline and demonstrating that sequence context provides complementary information beyond graph structure alone.
- **Sequence encoding strategy comparison.** We demonstrate that biologically informed statistical features outperform CNN-based one-hot encoding in this data regime, showing that handcrafted features encoding established determinants of methylation susceptibility are more effective than end-to-end sequence learning when training data is limited.
- **Biological interpretability.** Post-hoc analysis identifies CpG density and local adenine frequency as exhibiting age-dependent importance shifts consistent with known mechanisms of age-related hypermethylation, providing candidate biomarkers for aging intervention research.

2 Related Work

Epigenetic clocks. The field of epigenetic age prediction was established by landmark regression-based models that identified CpG sites whose methylation correlates linearly with chronological age [2, 3]. Subsequent research demonstrated that deep learning architectures could more effectively capture non-linear methylation dynamics: DeepMAge [7] utilized a four-layer feedforward network trained on blood methylation data, whereas AltMAge [8] extended this framework to a pan-tissue clock employing multilayer perceptrons and interpreting predictions through SHAP values. Shi et al. [15] proposed ResnetAge, a residual convolutional network that treats the ordered sequence of CpG beta values as a one-dimensional signal, achieving competitive performance across multiple tissue types. More recently, Prosz et al. [16] introduced XAI-AGE, a biologically informed, explainable deep neural network that incorporates pathway-level knowledge into its architecture, thereby illustrating that embedding biological structure within model design enhances both predictive accuracy and interpretability. Beyond chronological age prediction, second-generation clocks such as PhenoAge [17] have demonstrated that incorporating clinical biomarkers into methylation-based models yields stronger predictions of mortality and healthspan. Despite these advancements, a common limitation persists across all these methodologies: CpG sites are treated as independent features, with neither the relational structure among them nor the site-specific DNA sequence context that governs their methylation behaviour [18] taken into account.

Graph-based methylation modelling. To address the independence assumption, recent research has explored graph-based representations of methylation data. Wu et al. [11] developed co-methylation networks from RNA methylation data and demonstrated that modeling pairwise relationships among sites reveals functional associations that are not apparent in flat feature vectors. Building upon the graph paradigm, Ahmed et al. [9] introduced the first GNN-based epigenetic clock, named GraphAge, which represents CpG sites as nodes within a graph connected by co-methylation values, chromosomal proximity, and shared gene membership, and employs a PNA convolutional layer [19] for age regression. GraphAge demonstrated that integrating structural information among CpG sites improves both predictive accuracy and biological interpretability. Nevertheless, across all these graph-based approaches, node representations depend solely on methylation beta values and fixed positional attributes, leaving the local DNA sequence context of each CpG site completely unexploited [14].

Sequence context in methylation susceptibility. A separate line of research has established that the local DNA sequence environment is a primary determinant of CpG methylation susceptibility. Angermueller et al. [20] proposed DeepCpG, a convolutional neural network-based model designed to predict single-cell methylation states from local sequence windows, demonstrating that sequence motifs carry substantial predictive power for methylation variability [21, 22, 23, 24]. Santoni [12]

further showed that flanking sequence composition directly governs CpG methylation patterns, while Affinito et al. [13] demonstrated that nucleotide distance modulates co-methylation strength between proximal sites. Collectively, these findings establish that sequence context encodes complementary regulatory information that methylation values alone cannot capture [25].

Despite this evidence, no prior work has jointly integrated site-specific DNA sequence context and co-methylation graph structure within a unified epigenetic age prediction framework. Graph-based models exploit relational structure but ignore sequence context; sequence-aware models such as DeepCpG address methylation susceptibility but operate in the single-cell imputation setting and do not model population-level graph structure. Our work bridges this gap by proposing a unified sequence–graph integration framework with a lightweight gated modulation mechanism, systematically comparing handcrafted statistical features against CNN-based one-hot encoding in this data-limited setting, and evaluating against a comprehensive set of baselines spanning classical epigenetic clocks, deep learning age predictors, and graph-based methods.

3 Methods

We propose a unified sequence–graph integration framework for epigenetic age prediction that jointly models co-methylation graph structure and site-specific DNA sequence context via a lightweight gated modulation mechanism, followed by a PNA convolutional layer [19] and an MLP for age regression.

3.1 DNA Sequence Feature Extraction

For each CpG site, an eight-dimensional statistical feature vector is extracted from its surrounding genomic sequence. In contrast to methylation beta values, which exhibit inter-individual variability, these features represent intrinsic physicochemical and compositional properties of each CpG locus and are invariant across samples. Each dimension is designed to capture a distinct and biologically interpretable characteristic of the local sequence environment, as detailed in Table 1.

Table 1: Eight-dimensional DNA sequence statistical features extracted for each CpG site.

Dimension	Feature	Description
1	GC content	Proportion of G and C nucleotides in the full sequence
2	CpG density	Frequency of CG dinucleotides relative to sequence length
3	Upstream GC content	GC proportion in the 60 bp upstream of the CpG site
4	Downstream GC content	GC proportion in the downstream region
5	Local adenine frequency	Proportion of A in the 10 bp window surrounding the CpG site
6	Local thymine frequency	Proportion of T in the 10 bp window surrounding the CpG site
7	Local cytosine frequency	Proportion of C in the 10 bp window surrounding the CpG site
8	Local guanine frequency	Proportion of G in the 10 bp window surrounding the CpG site

3.2 Gated Modulation Architecture

As illustrated in Figure 1, the model combines two parallel input pathways, one extracting eight-dimensional DNA sequence statistical features and the other carrying methylation signals with positional attributes, that converge in the Sequence-Graph Integration Module before being passed through a GNN and MLP for age regression.

The model operates on a graph of $N = 20,318$ CpG sites. Each node i carries a ten-dimensional node feature vector comprising one methylation beta value and nine fixed positional attributes, and an eight-dimensional sequence statistical feature vector extracted from the 122 bp² surrounding genomic sequence. Each edge carries a three-dimensional attribute vector encoding co-methylation correlation, same-chromosome, and same-gene indicators. The sequence features are processed by two lightweight networks: an importance gate producing a scalar weight $g_i \in (0, 1)$, and a projection network producing a two-dimensional representation \mathbf{p}_i . The modulated methylation value $\tilde{m}_i = m_i \cdot g_i$ is concatenated with the positional attributes and \mathbf{p}_i to form a 12-dimensional fused node representation, passed through a PNA convolutional layer and an MLP for age prediction.

²Base pair (bp) is the fundamental unit of DNA length.

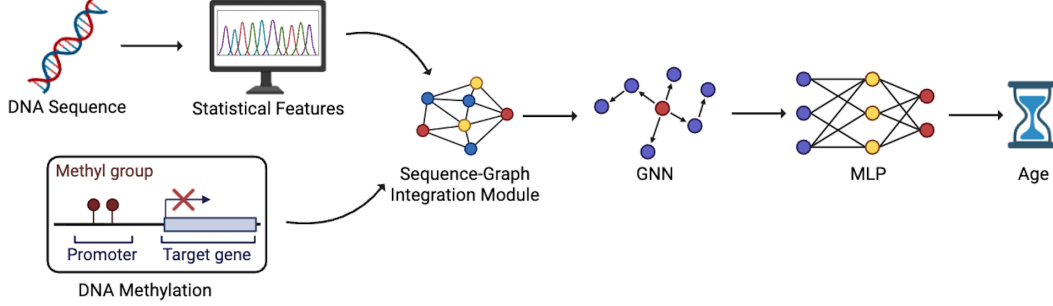


Figure 1: Overview of the proposed sequence–graph integration framework. Eight-dimensional DNA sequence features and methylation signals are fused via gated modulation, where methylation denotes methyl group addition at CpG sites in promoter regions that silences target genes. The fused representation is passed through a GNN and MLP for age regression.

Importance Gating. Given the sequence feature vector $\mathbf{s}_i \in \mathbb{R}^8$ for CpG site i , the importance gate computes a scalar modulation weight through a two-layer feedforward network with a sigmoid activation:

$$g_i = \sigma(W_2 \cdot \text{ReLU}(W_1 \mathbf{s}_i + \mathbf{b}_1) + b_2) \quad (1)$$

where $W_1 \in \mathbb{R}^{16 \times 8}$, $\mathbf{b}_1 \in \mathbb{R}^{16}$, $W_2 \in \mathbb{R}^{1 \times 16}$, $b_2 \in \mathbb{R}$ are learnable parameters, and $\sigma(\cdot)$ denotes the sigmoid function. The original methylation beta value $m_i \in \mathbb{R}$ is then modulated as:

$$\tilde{m}_i = m_i \cdot g_i \quad (2)$$

This formulation enables the model to differentially weight methylation signals according to their sequence-determined biological relevance, attenuating contributions from sites whose local sequence context confers limited age-predictive information while amplifying those associated with sequence environments characteristic of strong age-related methylation dynamics.

Sequence Projection. A secondary projection network maps the sequence feature vector to a two-dimensional representation that encodes complementary sequence-level information alongside the scalar gate, providing an explicit sequence-derived component within the fused node representation:

$$\mathbf{p}_i = W_4 \cdot \text{ReLU}(W_3 \mathbf{s}_i + \mathbf{b}_3) + \mathbf{b}_4 \quad (3)$$

where $W_3 \in \mathbb{R}^{8 \times 8}$, $\mathbf{b}_3 \in \mathbb{R}^8$, $W_4 \in \mathbb{R}^{2 \times 8}$, $\mathbf{b}_4 \in \mathbb{R}^2$ are learnable parameters.

Node Representation Fusion. The final node representation is constructed by concatenating three components:

$$\mathbf{x}_i = [\tilde{m}_i \parallel \mathbf{f}_i \parallel \mathbf{p}_i] \in \mathbb{R}^{12} \quad (4)$$

where $\mathbf{f}_i \in \mathbb{R}^9$ denotes the positional feature vector. This fusion explicitly combines sequence-derived information (\tilde{m}_i and \mathbf{p}_i) with graph-level positional attributes (\mathbf{f}_i) into a unified node representation before graph convolution, ensuring that both sequence context and structural information jointly inform the message passing process. The PNA aggregation for node i is defined as:

$$\mathbf{h}_i = \bigoplus_{(j,i) \in \mathcal{E}} \text{PNA}(\mathbf{x}_i, \mathbf{x}_j, \mathbf{e}_{ij}) \quad (5)$$

where \mathcal{E} denotes the edge set, $\mathbf{e}_{ij} \in \mathbb{R}^3$ is the edge feature vector between sites i and j , and \bigoplus denotes the combination of multiple aggregators (mean, max, min, and standard deviation), each scaled by identity, amplification, and attenuation scalars as defined in the original PNA formulation [19].

Age Regression. The output of the PNA layer $h_i \in \mathbb{R}$ is passed through a ReLU activation, yielding a scalar embedding per CpG site. The full embedding vector across all $N = 20,318$ CpG sites is passed through a multilayer perceptron (MLP) to produce the predicted age \hat{y}_k . The model is trained by minimising the mean squared error between predicted and true chronological age:

$$\mathcal{L} = \frac{1}{N_s} \sum_{k=1}^{N_s} (\hat{y}_k - y_k)^2 \quad (6)$$

where N_s is the number of training samples, \hat{y}_k is the predicted age, and y_k is the true chronological age of sample k . The MLP architecture and training configuration are detailed in Section 4.

4 Experiment

Dataset. All experiments are conducted on healthy blood methylation samples compiled from 37 publicly accessible datasets obtained from the NCBI Gene Expression Omnibus (GEO) [26] and EBI ArrayExpress [27]. All samples are measured using the Illumina HumanMethylation27 platform (GPL8490³), which covers 20,318 CpG sites common across platforms. The combined dataset comprises 3,707 healthy samples spanning an age range of 0 to 93 years, with a gender distribution of 37.4% male and 62.6% female. The age distribution is depicted in Figure 5 (Appendix A). From each individual dataset, 20% of samples are reserved as a held-out test set, resulting in 756 test samples. The remaining samples are partitioned using 5-fold cross-validation; training and evaluation are performed on fold 2, yielding 2,360 training samples and 591 validation samples. Full details of the CpG site annotation preprocessing, node feature construction, and graph construction procedure are provided in Appendix A.

Baselines. We evaluate two categories of baselines on the same held-out test set under identical data conditions.

Epigenetic clock baselines. We include five established epigenetic clocks spanning classical and deep learning approaches. Horvath [2] is a penalised linear regression model applied using its published coefficients. AltumAge [8] is a pan-tissue MLP-based clock applied using its published pre-trained weights. DeepMAge [7] and ResnetAge [15] are deep learning clocks whose weights are not publicly available; we re-implement their published architectures and retrain both under identical experimental conditions to ensure a fair comparison. GraphAge [9] reports a PNA-GNN result on the same platform and dataset split, included as an external reference point.

Controlled ablation variants. We compare three configurations differing only in sequence integration: PNA-GNN [9, 19], the sequence-agnostic baseline; PNA-GNN + CNN Sequence Encoding, using a three-layer 1D CNN to extract 32-dimensional sequence embeddings; and PNA-GNN + Statistical Features (Ours), using the eight-dimensional statistical features described above.

Evaluation Metrics. We report Mean Absolute Error (MAE) as the primary evaluation metric [2, 7, 8]. MAE provides a direct and interpretable measure of prediction accuracy in units of years and is less sensitive to outliers than Mean Squared Error (MSE). We additionally report MSE and the coefficient of determination (R^2) to characterise the overall alignment between predicted epigenetic age and true chronological age.

Implementation Details. The MLP consists of eight fully connected layers with output dimensions 1024, 656, 256, 124, 64, 32, 8, and 1, interleaved with ReLU and SELU [28] activations and dropout regularisation [29] ($p = 0.2$) at selected layers. The model is optimised using Adam [30] with learning rate 5×10^{-4} and weight decay 5×10^{-3} , with a ReduceLROnPlateau scheduler (patience = 4, factor = 0.4, minimum learning rate 10^{-8}) over 140 epochs. All experiments are conducted on an NVIDIA H100 GPU. Full hardware and training details are provided in Appendix B.

4.1 Comparison Against Epigenetic Clock Baselines

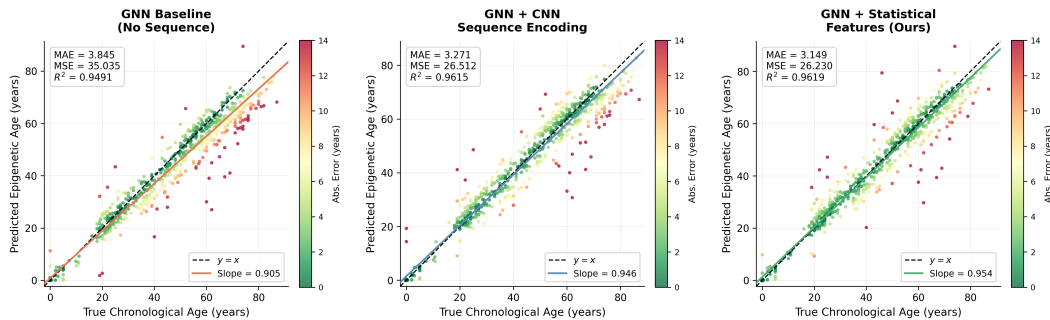
Table 2 presents the test set performance of all model configurations. Figure 2 visualises the alignment between predicted and true age across the three controlled sequence-graph integration variants.

Comparison with epigenetic clock baselines. Among the established epigenetic clocks evaluated on our test set, the classical linear regression model of Horvath [2] achieves MAE = 5.823, reflecting the well-known limitation of penalised linear models in capturing non-linear methylation-age relationships across diverse datasets. Deep learning clocks reduce this error substantially: AltumAge [8] achieves MAE = 3.710, and DeepMAge [7] achieves MAE = 3.222 when retrained on our dataset. ResnetAge [15], a residual convolutional architecture applied directly to the methylation beta value sequence, achieves MAE = 5.552. This indicates that one-dimensional convolutional processing of CpG site ordering is less effective than MLP-based approaches at this dataset scale, where the ordering of CpG sites does not encode biologically meaningful spatial structure. GraphAge [9]

³<https://www.ncbi.nlm.nih.gov/geo/query/acc.cgi?acc=GPL8490>

Table 2: Test set performance ($n = 756$).

Model	MAE↓	MSE↓	R^2 ↑
Horvath [2]	5.823	78.104	0.8865
AltumAge [8]	3.710	47.675	0.9307
DeepMAge [7]	3.222	29.574	0.9570
ResnetAge [15]	5.552	58.481	0.9150
GraphAge [9]	3.611	29.966	0.9564
PNA-GNN [9, 19]	3.845	35.035	0.9491
PNA-GNN + CNN Sequence Encoding	3.271	26.512	0.9615
PNA-GNN + Statistical Features (Ours)	3.149	26.230	0.9619

Figure 2: Predicted vs. true age for the three variants ($n = 756$).

achieves MAE = 3.611, demonstrating that graph-based modelling of co-methylation structure captures relational dependencies that are not exploited by sequence-based deep learning approaches such as ResnetAge [15]. Our proposed framework surpasses all established baselines with MAE = 3.149.

Contribution of sequence-graph integration. Under identical experimental conditions, jointly integrating DNA sequence statistical features with co-methylation graph structure reduces the test MAE from 3.845 to 3.149, an 18.1% improvement over the sequence-agnostic baseline. This gain reflects the complementary nature of the two information sources: graph structure captures relational dependencies among CpG sites, enabling each site to contextualise its methylation signal relative to functionally related neighbours, while sequence features provide site-specific biological priors that determine which methylation signals are age-relevant. Without sequence context, the model relies entirely on graph structure to discriminate age-related methylation changes from individual variation. In addition, without graph structure, sequence features cannot propagate regulatory context across functionally related sites. The gated modulation mechanism bridges the two by learning to weight each site’s methylation signal according to its sequence-determined biological relevance, enabling the integrated framework to selectively amplify signals from sites whose methylation dynamics are systematically coupled to the aging process.

Sequence encoding strategy. Comparing the two integration strategies, statistical feature extraction (MAE = 3.149) outperforms CNN-based one-hot encoding (MAE = 3.271). This result contradicts the common expectation that end-to-end learned representations should be more expressive than hand-crafted features, and can be explained by two key factors. First, the CNN encoder must learn to compress a 122×4 one-hot representation into a meaningful 32-dimensional embedding from only 2,360 training samples. Unlike methylation values, which vary across individuals and provide a dense supervision signal, the sequence for each CpG site is fixed and identical across all samples. The CNN therefore receives no per-sample feedback about which sequence patterns predict age, and can only learn from the aggregate statistical relationship between sequence motifs and methylation-based age prediction, a considerably weaker learning signal at this dataset scale. Second, the eight-dimensional statistical features directly encode biologically established determinants of methylation susceptibility, including GC content, CpG density, and local nucleotide composition, reflecting known DNA methyltransferase enzyme binding preferences [12, 13, 31] and CpG island

regulatory context [32]. These features condense well-established biochemical knowledge into a compact representation, eliminating the need for the model to rediscover these relationships from sequence data alone.

4.2 Age Group and Temporal Analysis

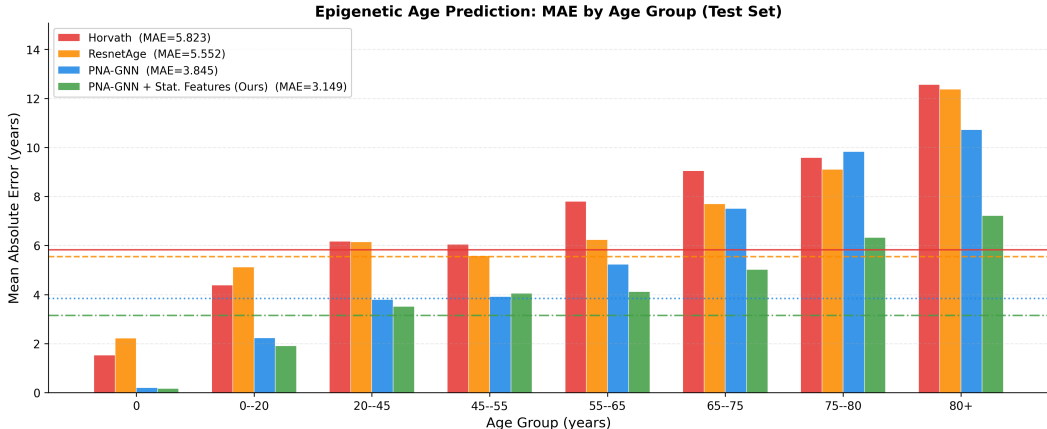


Figure 3: Test MAE by age group ($n = 756$).

Age group performance. Figure 3 presents the per-age-group MAE across four evaluated models. Our method achieves the lowest MAE in every age group, with prediction accuracy highest for neonatal subjects (MAE = 0.173 for age group 0) and degrading progressively with age, reaching MAE = 7.225 for subjects aged 80 and above. Horvath and ResnetAge show substantially higher errors across all age groups, while PNA-GNN remains competitive but is consistently outperformed by our method. This monotonic increase reflects a well-established biological phenomenon: in young subjects, epigenetic methylation patterns are tightly regulated and closely coupled to developmental programmes, resulting in a highly reproducible relationship between methylation and chronological age. As individuals age, stochastic epigenetic drift accumulates, causing methylation patterns to diverge progressively from the population mean [33]. This drift is driven by the progressive loss of youthful epigenetic information as described by the Information Theory of Aging [34], imperfect maintenance of methylation marks during DNA replication, and the cumulative effect of environmental exposures, all of which introduce noise that cannot be captured by any methylation-based clock [35]. The consequence is an inherent upper bound on prediction accuracy for older age groups that cannot be overcome through architectural improvements alone, since the biological signal itself becomes less reliable. Importantly, the age groups spanning 20 to 65 years, which constitute 55.2% of test samples, achieve MAE values between 3.5 and 4.2 years for our method, remaining close to the overall test MAE of 3.149 and confirming that the model generalises well across the most clinically relevant age range.

Alignment with chronological age. The scatter plots in Figure 2 illustrate a qualitative difference in model behaviour that is not fully reflected by the MAE values alone. The sequence-agnostic baseline demonstrates a notable regression-to-the-mean effect, as evidenced by a fit line slope of 0.905, indicating systematic underestimation of age in older individuals and overestimation in younger ones. This is a characteristic failure mode arising when node representations lack adequate discriminative power to differentiate the full dynamic range of methylation states. Without sequence context, the integrated framework cannot determine which CpG sites carry age-driven methylation signals versus those whose variation is attributable to individual differences unrelated to aging, resulting in conservative predictions that regress toward the training mean. CNN-based sequence encoding partially mitigates this, raising the slope to 0.946, though improvement is limited by the CNN’s inability to reliably extract informative sequence features at this dataset scale. Our statistical feature approach achieves the highest slope of 0.954, approaching the ideal value of 1.0, and produces the most compact point cloud around the diagonal. The R^2 values follow the same ordering (0.9491, 0.9615, 0.9619), confirming that jointly integrating sequence context and graph structure enhances the model’s capacity to capture the full dynamic range of epigenetic age.

4.3 Sequence Feature Interpretability via GNNExplainer

Sequence feature importance across the age spectrum. Figure 4 presents the temporal analysis of sequence feature importance scores across chronological age, using LOWESS regression to capture non-linear trends without imposing a parametric form. Pearson correlation coefficients are computed to characterise the overall direction and strength of each trend; features with $p > 0.01$ are shown without a smoothed curve. Linear regression results are provided in Appendix C for comparison.

Two features exhibit increasing importance across age groups, from younger to older individuals: CpG density ($r = 0.81$, $p < 0.001$) and local adenine frequency ($r = 0.71$, $p < 0.001$). The LOWESS curves reveal that this increase is non-linear: both features show a plateau or slight decline from childhood through adolescence (0–20 years), followed by a sustained increase through adulthood into old age. This pattern suggests that sequence-determined regulatory context becomes progressively more relevant as stochastic epigenetic drift accumulates, consistent with the known biology of aging: CpG density is a primary determinant of CpG island regulatory context, and age-related hypermethylation preferentially targets CpG-dense promoter regions [36].

Downstream GC content ($r = -0.53$, $p < 0.001$) exhibits a distinct non-linear decline: the LOWESS curve shows a sharp decrease in importance during the first decade of life, followed by stabilisation through adulthood. This suggests that flanking sequence composition is most discriminative in early development, where methylation patterns are tightly coupled to sequence context, but becomes less informative as epigenetic drift increasingly dominates in older subjects. Notably, all features exhibit elevated importance scores near birth, reflecting the distinctly structured methylation landscape of neonatal samples relative to older age groups. Local guanine frequency shows no significant trend ($p = 0.88$), contributing uniformly across the lifespan.

Site-level importance trajectories for individual CpG sites are shown in Appendix D. Full details of the GNNExplainer [37] aggregation procedure are provided in Appendix E.

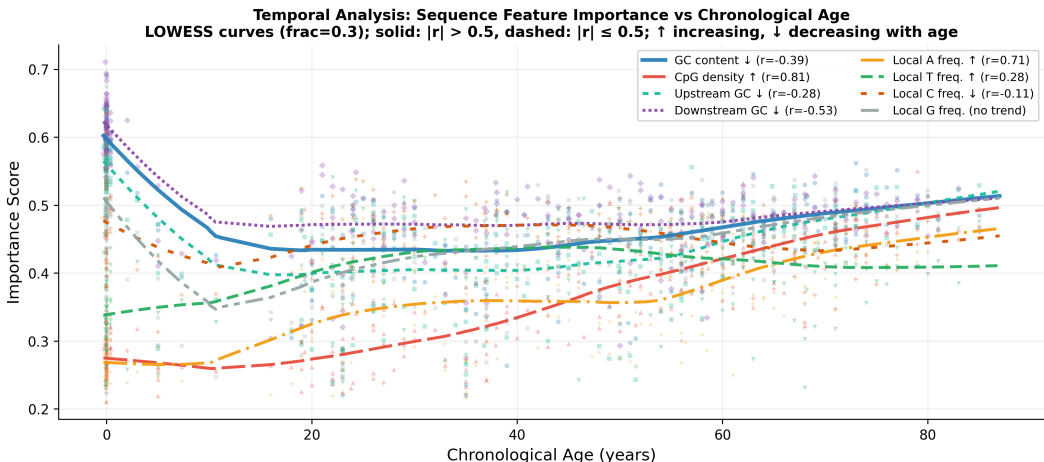


Figure 4: Temporal analysis of sequence feature importance scores.

5 Conclusion and Limitations

Conclusion. We proposed a unified sequence–graph integration framework for epigenetic age prediction that jointly models co-methylation graph structure and site-specific DNA sequence context via a lightweight gated modulation mechanism. Our framework achieves a test MAE of 3.149 years, surpassing all evaluated baselines including classical epigenetic clocks, deep learning age predictors, and graph-based methods, with a 12.8% improvement over the strongest graph-based baseline. Biologically informed statistical features outperform CNN-based sequence encoding, and post-hoc interpretability analysis reveals age-dependent importance shifts in CpG density and local adenine frequency consistent with known aging biology.

Limitations. All experiments are conducted on blood methylation samples from a single array platform (GPL8490⁴), and generalisation to other tissue types or higher-density arrays such as the 450K or EPIC platforms remains to be validated. Training is performed on a single cross-validation fold rather than averaging across all folds, which limits the statistical robustness of the reported performance estimates. The eight-dimensional sequence statistical features are derived from the reference genome and are therefore invariant across individuals, meaning the model cannot capture individual-specific sequence variation such as single nucleotide polymorphisms that may influence local methylation susceptibility. Finally, the GNNExplainer [37] interpretability analysis assigns importance scores in a post-hoc manner and reflects correlations between sequence features and model predictions rather than causal relationships. The identified age-dependent importance shifts in CpG density and local adenine frequency should therefore be treated as hypothesis-generating observations that warrant further experimental validation.

References

- [1] Rudolf Jaenisch and Adrian Bird. Epigenetic regulation of gene expression: how the genome integrates intrinsic and environmental signals. *Nature Genetics*, 33(Suppl):245–254, 2003. doi: 10.1038/ng1089.
- [2] Steve Horvath. DNA methylation age of human tissues and cell types. *Genome Biology*, 14(10):R115, 2013. doi: 10.1186/gb-2013-14-10-r115.
- [3] Gregory Hannum, Justin Guinney, Ling Zhao, Li Zhang, Guy Hughes, Srinivas Satta, Brandy Klotzle, Marina Bibikova, Jian-Bing Fan, Yuan Gao, Rob Deconde, Menzies Chen, Indika Rajapakse, Stephen Friend, Trey Ideker, and Kang Zhang. Genome-wide methylation profiles reveal quantitative views of human aging rates. *Molecular Cell*, 49(2):359–367, 2013. doi: 10.1016/j.molcel.2012.10.016.
- [4] Carlos López-Otín, Maria A. Blasco, Linda Partridge, Manuel Serrano, and Guido Kroemer. The hallmarks of aging. *Cell*, 153(6):1194–1217, 2013. doi: 10.1016/j.cell.2013.05.039.
- [5] Carlos López-Otín, Maria A. Blasco, Linda Partridge, Manuel Serrano, and Guido Kroemer. Hallmarks of aging: An expanding universe. *Cell*, 186(2):243–278, 2023. doi: 10.1016/j.cell.2022.11.001.
- [6] Steve Horvath and Kenneth Raj. DNA methylation-based biomarkers and the epigenetic clock theory of ageing. *Nature Reviews Genetics*, 19(6):371–384, 2018. doi: 10.1038/s41576-018-0004-3.
- [7] Fedor Galkin, Polina Mamoshina, Kirill Kochetov, Denis Sidorenko, and Alex Zhavoronkov. DeepMAge: A methylation aging clock developed with deep learning. *Aging and Disease*, 12(5):1252–1262, 2021. doi: 10.14336/AD.2020.1202.
- [8] Lucas Paulo de Lima Camillo, Louis R. Lapierre, and Ritambhara Singh. A pan-tissue DNA-methylation epigenetic clock based on deep learning. *npj Aging*, 8(1):4, 2022. doi: 10.1038/s41514-022-00085-y.
- [9] Saleh Sakib Ahmed, Nahian Shabab, Md Abul Hassan Samee, and M. Sohel Rahman. GraphAge: Unleashing the power of graph neural network to decode epigenetic aging. *PNAS Nexus*, 4(6):pgaf177, 2025. doi: 10.1093/pnasnexus/pgaf177.
- [10] Yasha Ektefaie, George Dasoulas, Ayush Noori, Maha Farhat, and Marinka Zitnik. Multimodal learning with graphs. *Nature Machine Intelligence*, 5(4):340–350, 2023. doi: 10.1038/s42256-023-00624-6.
- [11] Xiangyu Wu, Zhen Wei, Kunqi Chen, Qing Zhang, Jionglong Su, Hui Liu, Lin Zhang, and Jia Meng. m6Acomet: large-scale functional prediction of individual m6A RNA methylation sites from an RNA co-methylation network. *BMC Bioinformatics*, 20(1):223, 2019. doi: 10.1186/s12859-019-2840-3.

⁴<https://www.ncbi.nlm.nih.gov/geo/query/acc.cgi?acc=GPL8490>

- [12] Daniele Santoni. The impact of flanking sequence features on DNA CpG methylation. *Computational Biology and Chemistry*, 92:107480, 2021. doi: 10.1016/j.compbiolchem.2021.107480.
- [13] Ornella Affinito, Domenico Palumbo, Annalisa Fierro, Mariella Cuomo, Giulia De Riso, Antonella Monticelli, Gennaro Miele, Lorenzo Chiariotti, and Sergio Cocozza. Nucleotide distance influences co-methylation between nearby CpG sites. *Genomics*, 112(1):144–150, 2020. doi: 10.1016/j.ygeno.2019.05.007.
- [14] Francesco Di Giovanni, Lorenzo Giusti, Federico Barbero, Giulia Luise, Pietro Liò, and Michael Bronstein. On over-squashing in message passing neural networks: the impact of width, depth, and topology. In *Proceedings of the 40th International Conference on Machine Learning*, ICML'23. JMLR.org, 2023.
- [15] Lijuan Shi, Boquan Hai, Zhejun Kuang, Han Wang, and Jian Zhao. ResnetAge: A resnet-based DNA methylation age prediction method. *Bioengineering*, 11(1):34, 2024. doi: 10.3390/bioengineering11010034.
- [16] Aurel Prosz, Orsolya Pipek, Judit Börcsök, Gergely Palla, Zoltan Szallasi, Sandor Spisak, and Istvan Csabai. Biologically informed deep learning for explainable epigenetic clocks. *Scientific Reports*, 14:1306, 2024. doi: 10.1038/s41598-023-50495-5.
- [17] Morgan E. Levine, Ake T. Lu, Austin Quach, Brian H. Chen, Themistocles L. Assimes, Stefania Bandinelli, Lifang Hou, Andrea A. Baccarelli, James D. Stewart, Yun Li, Eric A. Whitsel, James G. Wilson, Alex P. Reiner, Abraham Aviv, Kurt Lohman, Yongmei Liu, Luigi Ferrucci, and Steve Horvath. An epigenetic biomarker of aging for lifespan and healthspan. *Aging*, 10(4): 573–591, 2018. doi: 10.18632/aging.101414.
- [18] Dirk Schübeler. Function and information content of DNA methylation. *Nature*, 517(7534): 321–326, 2015. doi: 10.1038/nature14192.
- [19] Gabriele Corso, Luca Cavalleri, Dominique Beaini, Pietro Liò, and Petar Veličković. Principal neighbourhood aggregation for graph nets. In *Advances in Neural Information Processing Systems*, volume 33, pages 13260–13271, 2020.
- [20] Christof Angermueller, Heather J. Lee, Wolf Reik, and Oliver Stegle. DeepCpG: accurate prediction of single-cell DNA methylation states using deep learning. *Genome Biology*, 18:67, 2017. doi: 10.1186/s13059-017-1189-z.
- [21] Eric Nguyen, Michael Poli, Marjan Faizi, Armin W. Thomas, Callum Birch Sykes, Michael Wornow, Aman Patel, Clayton Rabideau, Stefano Massaroli, Yoshua Bengio, Stefano Ermon, Stephen A. Baccus, and Christopher Ré. HyenaDNA: long-range genomic sequence modeling at single nucleotide resolution. In *Proceedings of the 37th International Conference on Neural Information Processing Systems*, NIPS '23, Red Hook, NY, USA, 2023. Curran Associates Inc.
- [22] Zhihan Zhou, Yanrong Ji, Weijian Li, Pratik Dutta, Ramana V. Davuluri, and Han Liu. DNABERT-2: Efficient foundation model and benchmark for multi-species genomes. In *International Conference on Learning Representations*, 2024.
- [23] Yair Schiff, Chia-Hsiang Kao, Aaron Gokaslan, Tri Dao, Albert Gu, and Volodymyr Kuleshov. Caduceus: bi-directional equivariant long-range DNA sequence modeling. In *Proceedings of the 41st International Conference on Machine Learning*, ICML'24. JMLR.org, 2024.
- [24] Frederikke Marin, Felix Teufel, Marc Horlacher, Dennis Madsen, Dennis Pultz, Ole Winther, and Wouter Boomsma. BEND: Benchmarking DNA language models on biologically meaningful tasks. In *International Conference on Learning Representations*, pages 15246–15281, 2024.
- [25] Bozhen Hu, Cheng Tan, Jun Xia, Yue Liu, Lirong Wu, Jiangbin Zheng, Yongjie Xu, Yufei Huang, and Stan Z. Li. Learning complete protein representation by dynamically coupling of sequence and structure. In *Advances in Neural Information Processing Systems*, volume 37, pages 137673–137697. Curran Associates, Inc., 2024.
- [26] National Center for Biotechnology Information. NCBI, 2024. URL <https://www.ncbi.nlm.nih.gov/>.

- [27] EMBL-EBI. EMBL’s European Bioinformatics Institute, 2024. URL <https://www.ebi.ac.uk/>.
- [28] Günter Klambauer, Thomas Unterthiner, Andreas Mayr, and Sepp Hochreiter. Self-normalizing neural networks. In *Proceedings of the 31st International Conference on Neural Information Processing Systems, NIPS’17*, pages 972–981, Red Hook, NY, USA, 2017. Curran Associates Inc.
- [29] Nitish Srivastava, Geoffrey Hinton, Alex Krizhevsky, Ilya Sutskever, and Ruslan Salakhutdinov. Dropout: A simple way to prevent neural networks from overfitting. *Journal of Machine Learning Research*, 15:1929–1958, 2014.
- [30] Diederik P. Kingma and Jimmy Ba. Adam: A method for stochastic optimization. In *International Conference on Learning Representations*, 2015.
- [31] Linfeng Gao, Max Emperle, Yiran Guo, Sara A. Grimm, Wendan Ren, Sabrina Adam, Hidetaka Uryu, Zhi-Min Zhang, Dongliang Chen, Jiekai Yin, Michael Dukatz, Hiwot Anteneh, Renata Z. Jurkowska, Jiuwei Lu, Yinsheng Wang, Pavel Bashtrykov, Paul A. Wade, Gang Greg Wang, Albert Jeltsch, and Jikui Song. Comprehensive structure-function characterization of DNMT3B and DNMT3A reveals distinctive de novo DNA methylation mechanisms. *Nature Communications*, 11(1):3355, 2020. doi: 10.1038/s41467-020-17109-4.
- [32] Aimée M. Deaton and Adrian Bird. CpG islands and the regulation of transcription. *Genes & Development*, 25(10):1010–1022, 2011. doi: 10.1101/gad.2037511.
- [33] Jean-Pierre Issa. Aging and epigenetic drift: a vicious cycle. *Journal of Clinical Investigation*, 124(1):24–29, 2014. doi: 10.1172/JCI69735.
- [34] Yuancheng Ryan Lu, Xiao Tian, and David A. Sinclair. The information theory of aging. *Nature Aging*, 3(12):1486–1499, 2023. doi: 10.1038/s43587-023-00527-6.
- [35] Meaghan J. Jones, Sarah J. Goodman, and Michael S. Kobor. DNA methylation and healthy human aging. *Aging Cell*, 14(6):924–932, 2015. doi: 10.1111/accel.12349.
- [36] Jean-Pierre Issa. CpG-island methylation in aging and cancer. *Current Topics in Microbiology and Immunology*, 249:101–118, 2000. doi: 10.1007/978-3-642-59696-4_7.
- [37] Zhitao Ying, Dylan Bourgeois, Jiaxuan You, Marinka Zitnik, and Jure Leskovec. GNNExplainer: Generating explanations for graph neural networks. In *Advances in Neural Information Processing Systems*, volume 32, pages 9240–9251, 2019.

A Dataset Details and Preprocessing

Sample filtering. Each dataset is filtered to retain only blood tissue samples. Samples with any missing methylation values are excluded. The resulting samples are restricted to the 20,318 CpG sites present in the AltumAge multi-platform CpG list [8]. All train/test splits are performed prior to any graph construction to prevent data leakage.

CpG site annotation preprocessing. Positional and biological attributes for each CpG site are loaded from the GPL8490 Illumina HumanMethylation27 manifest. Sites with missing chromosome assignments are removed. CpG island start and end positions are parsed from the island location field, with missing values defaulting to zero. CpG island length is computed as the difference between end and start positions. The following continuous attributes are normalised per chromosome using Min-Max scaling: genomic position, TSS coordinate, CpG island start and end positions, CpG island length, and distance to TSS. Missing distance-to-TSS values are filled with the maximum normalised value of 1 after scaling. The following categorical attributes are one-hot encoded: gene strand direction, next adjacent nucleotide, and source strand orientation.

Node feature construction. Each CpG site node carries a ten-dimensional feature vector. The first dimension is the sample-varying methylation beta value. The remaining nine dimensions are fixed positional attributes derived from the preprocessed manifest: CpG island membership, CpG island length, distance to TSS, next-base encoding spanning three dimensions, normalised CpG island start position, normalised CpG island end position, and normalised genomic coordinate.

Graph construction. The co-methylation graph is constructed separately for each cross-validation fold using only the fold’s training samples. This ensures no information from the validation or test sets influences the graph topology. Pearson correlation coefficients are computed across all pairs of 20,318 CpG sites using training-fold methylation beta values. An edge between sites i and j is included under any of the following conditions, with self-loops excluded. First, the absolute correlation $|r_{ij}|$ exceeds 0.70, regardless of chromosome. Second, sites i and j are on the same chromosome and $|r_{ij}|$ exceeds 0.68. Third, sites i and j are on the same chromosome, their genomic distance is less than 10^5 bp, and $|r_{ij}|$ exceeds 0.66. Each edge carries a three-dimensional attribute vector encoding the Pearson correlation coefficient, a same-chromosome binary indicator, and a same-gene binary indicator.

DNA sequence feature extraction. The 122 bp surrounding genomic sequence for each CpG site is retrieved from the platform manifest. The CpG dinucleotide marker is standardised and all characters are uppercased prior to feature extraction. Unknown nucleotides are assigned equal probability across all four bases. All sequence features are invariant across samples and are computed once prior to training. The eight-dimensional statistical feature vector is described in Table 1.

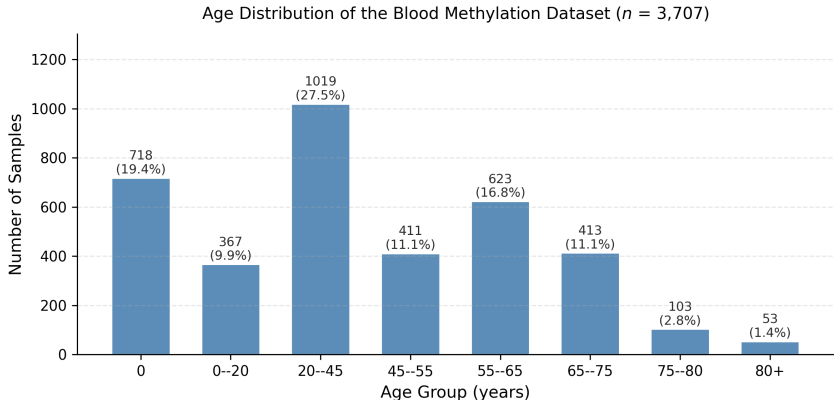


Figure 5: Age distribution of the blood methylation dataset ($n = 3,707$).

B Hardware and Training Details

All experiments are conducted on a single NVIDIA H100 GPU. Total training time for fold 2 is approximately 9 hours. A batch size of 1 is used throughout training. A fixed random seed of 0 is applied to Python, NumPy, and PyTorch to ensure reproducibility.

C Linear Regression Temporal Analysis

Figure 6 presents linear regression fits of sequence feature importance scores across chronological age, complementing the LOWESS analysis in Figure 4. The linear fits confirm the directional trends identified by LOWESS. CpG density exhibits a statistically significant positive slope with $r = 0.81$. Local adenine frequency also shows a significant positive slope with $r = 0.71$. Downstream GC content shows a significant negative slope with $r = -0.53$. GC content and upstream GC content show weak negative trends with $r = -0.39$ and $r = -0.28$ respectively. Local thymine frequency shows a weak positive trend with $r = 0.28$. Local guanine and cytosine frequencies show no significant linear trend.

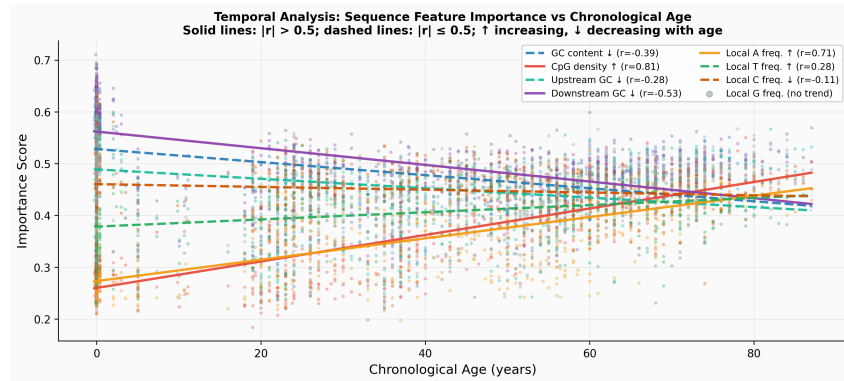


Figure 6: Linear regression fits of sequence feature importance scores across chronological age.

D CpG Site-Level Importance Trajectories

Figure 7 presents node-level importance trajectories for the top 10 CpG sites with increasing and decreasing importance across chronological age. Sites with increasing importance are associated with genes involved in neuronal signalling and metabolic regulation. This suggests that sequence-regulatory context at these loci becomes progressively more discriminative for age prediction with advancing age. Sites with decreasing importance are associated with genes implicated in cytoskeletal organisation and mitochondrial function. This is consistent with their methylation patterns being most informative during early development and less so in older subjects.

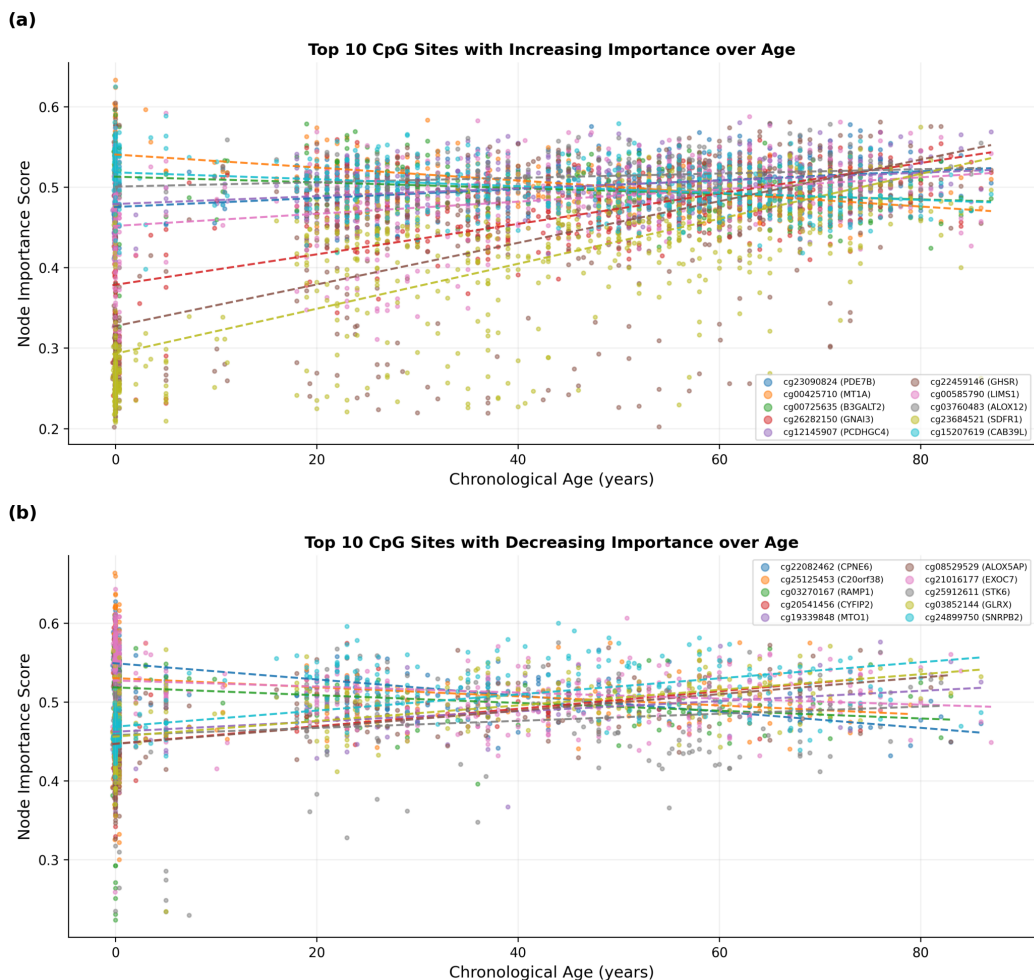


Figure 7: Top 10 CpG sites with increasing (a) and decreasing (b) node importance scores across chronological age, fitted with linear regression.

E GNNExplainer Aggregation Details

Post-hoc interpretability analysis is conducted using GNNExplainer [37] applied to all 756 test samples independently. Two complementary analyses are performed.

Sequence feature importance. GNNExplainer is applied with a shared attribute mask setting, which directly produces a single eight-dimensional importance vector that is common across all 20,318 CpG site nodes within each sample. This formulation does not require aggregation across nodes. The importance vector reflects the contribution of each sequence statistical feature to the model prediction at the graph level. Per-sample importance vectors are averaged across all 756 test samples to obtain the mean importance score for each feature. For the temporal analysis in Figure 4, the per-sample importance vectors are regressed against the corresponding chronological age using Pearson correlation to characterise age-dependent importance trends.

CpG site-level importance. GNNExplainer is applied with a per-node scalar mask setting, producing an independent scalar importance score for each of the 20,318 CpG site nodes per sample. This yields a matrix of shape $756 \times 20,318$ containing per-sample per-node importance scores. For each CpG site, a linear regression is fitted between its importance scores across all 756 samples and the corresponding chronological ages. The resulting slope is used to rank sites by their age-dependent importance trend.